

# LJMU Research Online

Baxter, T and Kobayashi, S

Probing the axial symmetry of gamma-ray burst jets using afterglow polarimetry

https://researchonline.ljmu.ac.uk/id/eprint/27519/

## Article

**Citation** (please note it is advisable to refer to the publisher's version if you intend to cite from this work)

Baxter, T ORCID logoORCID: https://orcid.org/0009-0004-4738-9022 and Kobayashi, S ORCID logoORCID: https://orcid.org/0000-0001-7946-4200 (2025) Probing the axial symmetry of gamma-ray burst jets using afterglow polarimetry. Monthly Notices of the Royal Astronomical Society. 543 (2). pp.

LJMU has developed LJMU Research Online for users to access the research output of the University more effectively. Copyright © and Moral Rights for the papers on this site are retained by the individual authors and/or other copyright owners. Users may download and/or print one copy of any article(s) in LJMU Research Online to facilitate their private study or for non-commercial research. You may not engage in further distribution of the material or use it for any profit-making activities or any commercial gain.

The version presented here may differ from the published version or from the version of the record. Please see the repository URL above for details on accessing the published version and note that access may require a subscription.

For more information please contact <a href="mailto:researchonline@ljmu.ac.uk">researchonline@ljmu.ac.uk</a>



MNRAS 543, 1039-1047 (2025) Advance Access publication 2025 September 15

# Probing the axial symmetry of gamma-ray burst jets using afterglow polarimetry

Thomas Baxter <sup>0</sup>★ and Shiho Kobayashi

Astrophysics Research Institute, Liverpool John Moores University, IC2, Liverpool Science Park, 146 Brownlow Hill, Liverpool L3 5RF, UK

Accepted 2025 September 8. Received 2025 August 12; in original form 2025 March 10

#### **ABSTRACT**

Polarization measurements of gamma-ray burst afterglows provide a powerful tool for probing the structure of relativistic jets. In this study, we revisit polarization signals observed in gamma-ray burst afterglows, focusing on the effects of non-axisymmetric jet structures. To characterize these non-axisymmetric jets, we adopt a simple elliptical jet head model and investigate how deviations from axisymmetry influence the temporal evolution of polarization properties, particularly around the jet break. Our results show that the polarization degree curve typically exhibits two peaks for top-hat jets or a single peak for structured jets, even in the presence of an elliptical jet head. In non-axisymmetric jets, a complete drop in polarization between peaks is generally absent, and the position angle rotation between the peaks can deviate significantly from 90 deg. In single-peak cases, the polarization position angle evolves gradually, contrasting with the constant position angle expected in axisymmetric jets. We also explore the implications of these findings for recent gamma-ray burst (GRB) events, including GRB 121024A, GRB 091018, GRB 020813, and GRB 210610B.

**Key words:** magnetic fields – polarization – radiation mechanisms: non-thermal – relativistic processes – gamma-ray bursts..

### 1 INTRODUCTION

The afterglow of a gamma-ray burst (GRB) emerges as the relativistic jet decelerates due to its interaction with the surrounding circumburst material. This interaction generates a forward shock that propagates as a collimated blast wave. Electrons accelerated within these shocks produce the observed non-thermal emission via synchrotron radiation (Sari, Piran & Narayan 1998).

The simple top-hat jet model has been remarkably successful in explaining many GRB afterglow observations. This success stems from the fact that, for an on-axis observer, the emission from the jet core dominates, resulting in an afterglow light curve that shows no distinct features indicative of the jet's structure. However, the groundbreaking gravitational-wave-triggered detection of a binary neutron star merger, linked to GRB 170817A (Abbott et al. 2017), demonstrated that the afterglows of off-axis events are highly sensitive to the structure of the jet (e.g. Lamb & Kobayashi 2017). Observations have shown that the late-time afterglow light curve of GRB 170817A is consistent with Gaussian jet models (Lazzati et al. 2018; Margutti et al. 2018; Ghirlanda et al. 2019; Lamb et al. 2019; Troja et al. 2019). Meanwhile, a shallow angular profile in relativistic jet models (e.g. power-law jets) has been proposed for GRB 221009A, the brightest burst ever observed (Burns et al. 2023; Lesage et al. 2023). The observed monochromatic steepening of the X-ray and optical light curves strongly suggests a geometrical effect, such as a jet break, although the post-break decay rates are shallower than expected. This discrepancy can be resolved if the afterglow

Numerical simulations suggest such jet structures can arise from the interaction between the jet and the confining medium (Gottlieb, Nakar & Bromberg 2021). Specifically, this occurs as the jet breaks out through the stellar envelope in the collapsar model (e.g. Zhang, Woosley & MacFadyen 2003; Lazzati & Begelman 2005; Gottlieb et al. 2021); or interacts with merger ejecta (e.g. Perego et al. 2014; Nativi et al. 2022). While most afterglow studies to date have focused on axisymmetric jets (either top-hat or structured), some have investigated azimuthal asymmetries in the energy and velocity distributions. An early example is Nakar & Oren (2004), who examined polarization signals in the patchy-shell model, demonstrating that angular inhomogeneities in an expanding shock can lead to lightcurve variability, accompanied by continuous, correlated changes in both the polarization degree and position angle. More recently, Li et al. (2023, 2024), discuss azimuthal energy and velocity inhomogeneities produced by internal non-uniform magnetic dissipation processes or the precession of the central engine (Huang et al. 2019). Recent 3D hydrodynamic simulations of jets in the aftermath of neutron star mergers (Gottlieb et al. 2022; Lamb et al. 2022) further highlight these complexities. These studies show that when a jet breaks out of the ejecta, the resulting outflow exhibits a power-lawlike polar energy distribution with rotational inhomogeneity. Notably, the jet head is not perfectly circular, as often assumed in conventional theoretical models, instead, it tends to exhibit a more elliptical shape.

Non-axisymmetric or inhomogeneous structures have been primarily discussed in the context of prompt gamma-ray emission (e.g. Lazar, Nakar & Piran 2009; Gill & Granot 2024). This emission originates from the original ejecta from the central engine, which

emission originates from a structured jet with a shallow angular energy profile (O'Connor et al. 2023; Birenbaum et al. 2024).

<sup>\*</sup> E-mail: aritbaxt@ljmu.ac.uk

carries large-scale magnetic fields generated at the central source. In contrast, the magnetic fields in the afterglow-emitting blast wave are thought to originate from shock-driven instabilities, resulting in a highly tangled structure whose properties are largely governed by the anisotropy of the post-shock field. Detailed afterglow light-curve modelling can break degeneracies between jet structure, viewing geometry, and magnetic field anisotropy (Gill & Granot 2020).

Although the mechanisms behind the acceleration and collimation of GRB jets remain uncertain, understanding their structures can provide valuable insights into these processes. This paper explores how jet asymmetries can be constrained through polarization observations of afterglows. Our study is partly motivated by recent polarization measurements of GRB 210610B (Agüí Fernández et al. 2024), which revealed a polarization position angle (PPA) rotation of  $\Delta \phi = 54^{\circ} \pm 9^{\circ}$  around a possible jet break (see Section 5.4 for details). This rotation deviates significantly from  $\Delta \phi = 90^{\circ}$  predicted for axisymmetric jets (Ghisellini & Lazzati 1999; Sari 1999).

We aim to investigate how jet axial asymmetry leaves an imprint on the temporal evolution of afterglow polarization. To break axisymmetry, we model the global jet structure with an elliptical head. Jets emerging from a collapsing star are unlikely to naturally form an elliptical head, as this would require a non-axisymmetric stellar structure; in reality, stars are typically axisymmetric around their rotational axis. In double neutron-star mergers, however, the ejecta along the rotational axis originates from the neutron star collision and may display non-axisymmetric features. Nevertheless, it is worth exploring deviations from axisymmetry, since a perfectly circular jet head is itself an idealised case.

We do not claim that GRB jets generally have elliptical heads. Rather, we adopt this geometry as a toy model to explore departures from the standard top-hat jet. While there is no strong physical motivation for explicitly elliptical heads, the eccentricity provides a simple parameter to control the degree of asymmetry in the global jet structure. This serves as a straightforward starting point for investigating non-axisymmetric jets in this context.

We present our model for evaluating polarization signals around a jet break in Section 2, where we illustrate the primary polarization signature of a non-axisymmetric jet. We describe the distributions of polarization signals when the line of sight of an observer intersects the jet head (or shock surface) at random locations in Section 3. In Section 4, we discuss the structured model in the context of non-axisymmetric jets. In Section 5, we present case studies. Finally, in Section 6, we give our conclusions and discussion.

# 2 POLARIZATION BEHAVIOUR AT A JET BREAK

In the afterglow phase, magnetic fields in the blast wave are believed to be produced by shock instabilities, though the precise mechanisms responsible for their production in relativistic collisionless shocks remain poorly understood. Since the shock normal (aligned with the radial direction) represents a distinct orientation, the magnetic field components parallel and perpendicular to the shock normal could exhibit significantly different average strengths (Ghisellini & Lazzati 1999; Medvedev & Loeb 1999; Sari 1999). While many models assume that the post-shock field lies entirely within the shock plane, some observations indicate a more isotropic geometry (Gill & Granot 2020; Stringer & Lazzati 2020).

Due to relativistic beaming, an observer at early times can only see a small portion of the jet head's surface. This visible region is confined to a small area with an angular size of  $1/\Gamma$ , centred around

the point where the line of sight intersects the jet head. Especially, at high frequencies (above the peak synchrotron frequency), most of the emission arises from a ring-like structure, caused by the relativistic limb-brightening effect (Granot, Piran & Sari 1999). Each small segment of the ring might produce highly polarized radiation due to the local anisotropy in the magnetic field, as discussed. However, the overall symmetry of the ring results in a net polarization of zero.

As noted independently by Sari 1999 and Ghisellini & Lazzati 1999, net polarization signals are expected to emerge around the time of a jet break, when the expanding visible region (i.e. the ring) begins to extend beyond the edge of the jet. We here revisit the polarization signals for a non-axisymmetric homogeneous (top-hat) jet.

Following Sari 1999, we adopt a toy model to approximate the evolution of the polarization signal. In this model, (1) the jet head is represented by an ellipse with eccentricity e, and the half-opening angle of the jet, particularly along the semimajor axis, is denoted by  $\theta_i$ . (2) Recent numerical hydrodynamic simulations suggest that lateral jet expansion occurs much more slowly than previously estimated (e.g. Granot & Piran 2012). Thus, we assume the lateral expansion is negligible, meaning both the jet opening angle and eccentricity remain constant. The Lorentz factor of the fluid is related to the observer time t by  $t/t_i = (\theta_i \Gamma)^{-8/3}$ , where  $t_i$  is the characteristic time for a jet break. (3) The (main) visible region is modelled as a thin ring with a radius of  $\Gamma^{-1}$ , centred on the point where the line of sight intersects the jet head. The ring's width is set to 30 per cent of its radius. (4) The emission from each fluid element within the ring is polarized in the local radial direction (i.e. perpendicular to the ring) with a polarization degree of  $P_0$ . This polarization direction assumes that the magnetic field component parallel to the shock normal dominates over the perpendicular component. If the parallel component were weaker, the Stokes parameters Q and U would change sign in the subsequent discussion. However, the discussion is basically identical. (5) The inner region of the ring, corresponding to a circular area with a radius of 0.7  $\Gamma^{-1}$ , emits much dimmer radiation - 10 per cent of the ring's brightness - and is assumed to be unpolarized. (6) Only the portion of the visible region (the ring and the inner circular area) that overlaps with the jet emits photons, uniformly distributed within each area. The region outside the jet does not contribute any emission. Under these assumptions, the evolution of polarization over time depends on the location of the observer's line of sight within the jet head, characterized by two parameters: the azimuthal angle from the semimajor,  $\chi$ , and the offset between the observer's line of sight and the centre of the jet, measured in units of the jet opening angle,  $\xi = \theta_{\text{view}}/\theta_{\text{i}}$ .

To estimate the Stokes parameters: Q and U, we divide the visible region (the ring and the inner circle) into many segments. Since we consider synchrotron emission from an optically thin blast wave, the circular polarization is zero V=0. Each segment contributes to Q and U as

$$dQ = P_{\rm e}dL\cos(2\phi_{\rm e}),\tag{1}$$

$$dU = P_e dL \sin(2\phi_e), \qquad (2)$$

where the local polarization degree  $P_{\rm e}=P_0$  when the segment lies within the ring, and  $P_{\rm e}=0$  when the segment is inside the inner circle. The local luminosity, dL, is proportional to the area of the segment while also incorporating the constraints imposed by conditions (3), (5), and (6) in the previous paragraph. The angle  $\phi_{\rm e}$  denotes the angle between the positive x-axis (the semimajor axis) and the segment's position vector, measured relative to the line of sight (Point A in Fig. 1). Considering condition (6),  $\Sigma dQ$ ,  $\Sigma dU$ ,

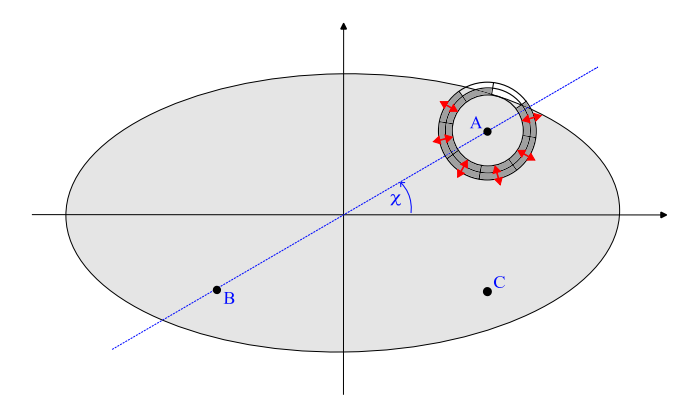


**Figure 1.** The shaded area represents the physical extent of the jet head, with the line of sight intersecting it at Point A. The location of Point A is specified by two angles: viewing angle  $\theta_{\text{view}}$ , measured from the jet axis (or equivalently expressed as  $\xi = (\theta_{\text{view}}/\theta_{\text{j}})$ , and the azimuthal angle  $\chi$ , measured from the semimajor axis of the jet head. The ring surrounding Point A marks the visible region. Red double-headed arrows indicate the polarization directions of fluid element emission. The point symmetric to Point A with respect to the jet axis (the origin) is Point B, while the point symmetric to Point A with respect to the *x*-axis is labelled Point C.

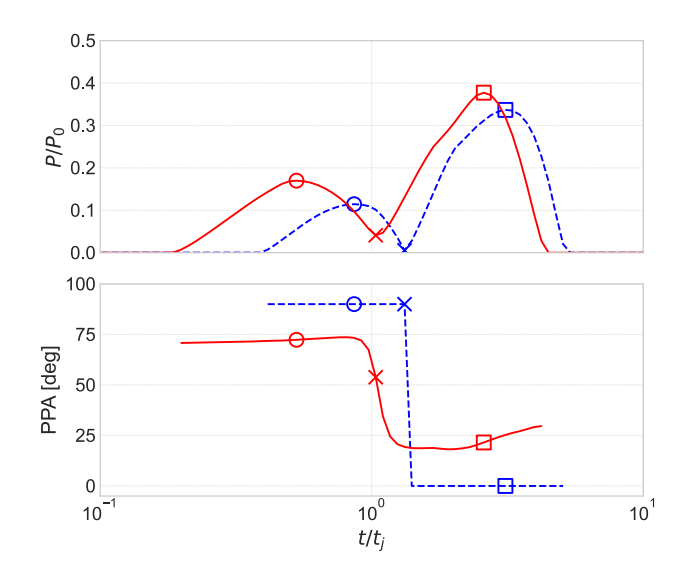


**Figure 2.** Top panel: polarization as a function of time, with both quantities normalized to the the local polarization degree  $P_0$  and the characteristic jetbreak time  $t_j$ , for e = 0 (blue dashed) and 0.6 (red solid). The first peaks, the troughs, and second peaks in the polarization light curves are marked by circles, crosses, and squares, respectively. The line of sight is characterized by  $\chi = 1$  and  $\xi = 0.3$ . Bottom panel: same as the top panel, but showing the the temporal evolution of the polarization position angle (PPA).

and  $\Sigma dL$  are evaluated to estimate the net values of the parameters:  $q = \Sigma dQ/\Sigma dL$  and  $u = \Sigma dU/\Sigma dL$ . The net polarization degree P and position angle  $\phi$  are given by

$$P = \sqrt{q^2 + u^2},\tag{3}$$

$$\phi = \frac{1}{2}\arctan(u/q). \tag{4}$$

Fig. 2 illustrates the differences in polarization signals between axisymmetric jets and non-axisymmetric jets (in this paper, non-axisymmetric jets refer to those with elliptical-shaped heads). For axisymmetric jets, the polarization degree curve (shown as the blue

dashed line in the top panel) exhibits two peaks, with the polarization dropping to zero between the peaks around the jet break time. As seen in the bottom panel, the PPA  $\phi$  rotates precisely by  $\pi/2$  before and after the point where polarization vanishes (Ghisellini & Lazzati 1999; Sari 1999). In contrast, jets with elliptical heads generally do not exhibit a complete polarization drop between the two peaks ( $P \neq 0$  at the trough). The PPA rotates more smoothly, though it still undergoes rapid changes near the trough (approximately at the jet break time). The change in PPA between the two peaks can significantly deviate from  $\pi/2$ ; in this example, it is approximately  $\Delta \phi = 0.28\pi \sim 50.4$  degrees (it is more convenient to express angles in radians for theoretical discussion, while degrees are preferred in the context of observations. Unless otherwise specified, angles are given in radians).

# 3 THE CHARACTERIZATION OF POLARIZATION SIGNALS

Consider an observer whose line of sight intersects a jet head, which is characterized by an eccentricity e, at the point  $(\chi, \xi)$ . This intersection point is labelled as Point A in Fig. 1. To characterize the time evolution of the PPA, we examine the PPA rotation  $\Delta\phi$  between two polarization peaks and the ratio  $R_{\rm pd}=P_{\rm 1st}/P_{\rm tr}$ , which quantifies the polarization degrees at the first peak relative to the trough. In Fig. 2, circles and squares denote these polarization peaks around a jet break. In particular, we analyse  $|\Delta\phi-\pi/2|$ , which measures deviations from the expected  $\pi/2$  rotation in axisymmetric jets. As discussed in Section 2, non-axisymmetric jets generally do not exhibit a complete polarization drop between the two peaks, resulting in lower values of  $R_{\rm pd}$ .

We investigate the distribution of polarization signals under the assumption that the intersection points of an observer's line of sight with the jet head are uniformly distributed. Due to the symmetry of the system, it is unnecessary to sample the entire ellipse  $(-\pi < \chi < \pi)$ ; instead, it is sufficient to consider a single quadrant  $(0 < \chi < \pi/2)$ .

To illustrate this, we first introduce Point B, which is symmetric to Point A with respect to the origin. The distribution of fluid elements around Point B (or the relative position of the jet edge) is identical to that around Point A when rotated by  $\pi$  around Point B. Consequently, given the angular dependences in equations (1) and (2), the polarization signals at any given time are therefore identical for Points A and B.

Similarly, consider Point C, which is symmetric to Point A with respect to the *x*-axis. The fluid element distribution around Point C mirrors that of Point A but with a reflection of  $\phi \leftrightarrow -\phi$  (flipping vertically with respect to the line passing through Point A and parallel to the *x*-axis). While the absolute values of the Stokes parameters at Point C match those at Point A, one of them flips sign, specifically (q, -u). Nevertheless, the position angle rotation  $|\Delta \phi - \pi/2|$  and the ratio  $R_{\rm pd}$  remain the same as at Point A.

To investigate intrinsically non-axisymmetric outflows, we model the asymmetric emitting surface with an elliptical cross-section, recovering a conical jet when the eccentricity of the jet head is zero, while assuming that the surface dynamics (i.e. the radial motion of each fluid element) still follow the relativistic expansion described by the Blandford–McKee solution. As a result, the emitting surface possesses curvature. The ellipse represented in Fig. 2 represents the projection of the jet head on to the sky. The opening angle of GRB jets or their core size is typically only several degrees. For such small angles, uniform sampling over projected area is approximately

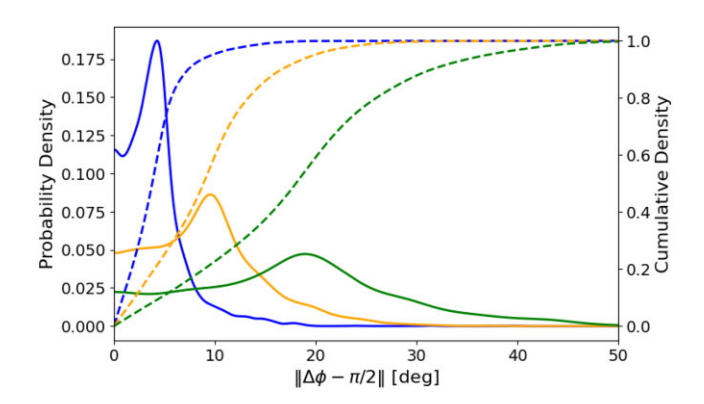


**Figure 3.** Distribution functions of deviations from  $\pi/2$  in the PPA rotation between polarization peaks for uniformly sampled jets with eccentricities of e=0.3 (blue lines), e=0.45 (orange lines), and e=0.6 (green lines). Solid lines represent probability density distributions, while dashed lines show their corresponding cumulative distributions.

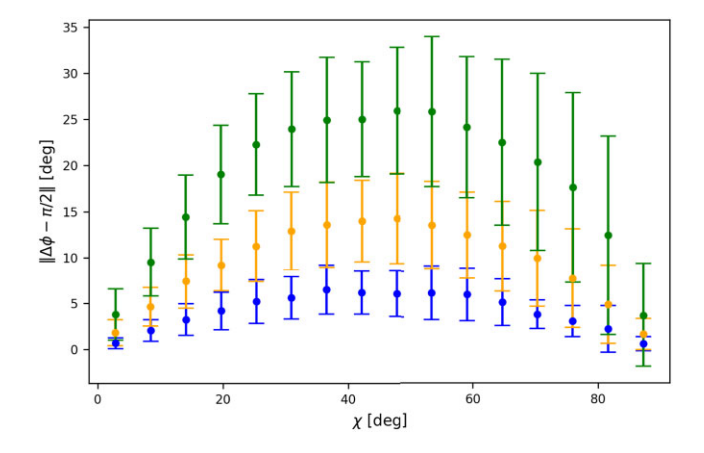


**Figure 4.** The PPA deviations from  $\pi/2$  are shown in 16 bins of equal angular width  $\chi$  for jets with eccentricities e=0.3 (blue), e=0.45 (orange), and e=0.6 (green). The dot represent the averaged values, and the bars indicate the  $1\sigma$  spreads for each bin.

equivalent to uniform sampling over the solid angle of the emitting surface.

Fig. 3 shows the distributions of  $|\Delta \phi - \pi/2|$ , derived from 5000 uniform sampled line-of-sight realizations across a quadrant of the elliptic jet head for eccentricity e = 0.3, 0.45, and 0.6. For axisymmetric jets (e = 0), the probability distribution is given by a delta function at 0, meaning the PPA rotation  $\Delta \phi$  is always  $\pi/2$ . As eccentricity increases, the probability distribution (solid lines) peaks at larger deviation angles, with the distribution's spread also increasing. The probability density distributions peak at  $|\Delta \phi - \pi/2|$ = 4.3, 9.5, and 19 deg, while their cumulative distributions reach 50 per cent at 3.8, 8.9, 18 deg, and 90 per cent at 7.3, 17, 31 deg for e = 0.3, 0.45, and 0.6, respectively. Since the semiminor axis is smaller than the semimajor axis by a factor of  $\sqrt{1-e^2}$ , it is reduced by approximately 5 per cent-20 per cent (or equivalently by a factor of  $\sim 0.8 - 0.95$ ) across this range of eccentricities. Our results show that even a mild deformation of the jet head leads to PPA rotations that deviate significantly from  $\pi/2$ .

When the line of sight intersects the jet head near its semimajor or semiminor axis, the geometry exhibits greater symmetry, leading to a position angle rotation close to  $\pi/2$ . As expected, Fig. 4 shows that the deviation from  $\pi/2$  increases with higher eccentricity, particu-

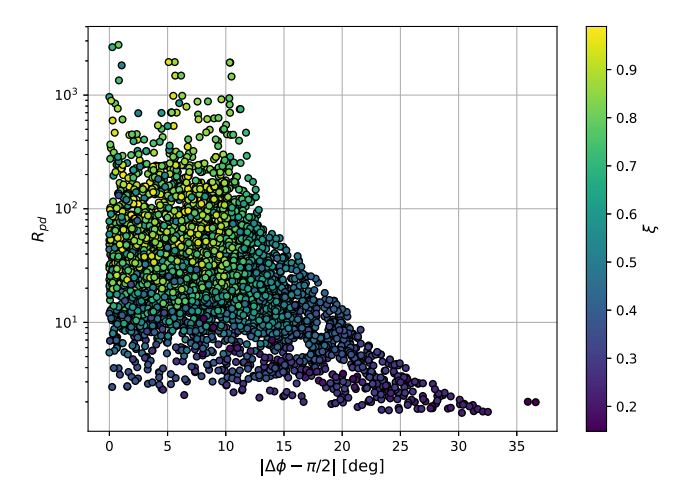


**Figure 5.** The deviation of the PPA rotation from  $\pi/2$  and the peak-to-trough ratio  $R_{\rm pd}$  are shown for the same random sample (e=0.45) that generates the orange lines in Fig. 3. The colour map indicates the offset  $\xi$  value of each sample.

larly for intermediate angles ( $\chi \sim \pi/4$ ). The spread in the probability distributions shown in Fig. 3 can be partly attributed to variations in PPA rotation between the more symmetric configurations ( $\chi \sim 0$  or  $\pi/2$ ) and the asymmetric configuration ( $\chi \sim \pi/4$ ). In Fig. 4, for e=0.6, the azimuthal bin nearest the semiminor axis ( $\chi \sim 90$  deg) results in negative values for  $1\sigma$  error. This is due to the significant positive skewness of the distribution.

Additionally, the offset  $\xi = \theta_{\text{view}}/\theta_{\text{i}}$  also influences the rotation of the position angle. Fig. 5 shows  $|\Delta \phi - \pi/2|$  and  $R_{\rm pd}$  for the same random uniform samples with e = 0.45, where the colour map represents the offset  $\xi$  for each sample. For a smaller offset (and intermediate  $\chi$ ), the deviation  $|\Delta \phi - \pi/2|$  becomes larger (if the line of sight passes regions near the semimajor or semiminor axis, the rotation is close to  $\pi/2$  regardless of the offset values). The high-deviation tails in the probability density distributions (the solid lines), seen above their peaks in Fig. 3, correspond to low- $\xi$  cases  $(\xi \lesssim 0.4)$  where the line of sight is relatively close to the central jet axis. At small offsets  $\xi$ , the first peak of the polarization curve becomes less pronounced, leading to a lower  $R_{pd}$ . For eccentricity e = 0.3, 0.45, and 0.6, the top 10 per cent of cases with the largest  $\Delta \phi$  deviation from  $\pi/2$  have  $R_{\rm pd}$  values below approximately 86, 38, and 22. Although these extreme cases show lower  $R_{\rm pd}$  for higher eccentricities, a jet head with a larger eccentricity e has a higher probability of producing a significant  $\Delta \phi$  deviation from  $\pi/2$ . As discussed in Section 5.4, observational measurements of  $R_{pd}$  and  $\Delta \phi$  can provide valuable constraints on the eccentricity e.

For even smaller offsets, one of the peaks, typically the first, becomes less pronounced. To determine whether a polarization curve exhibits two peaks and to locate them, we have implemented a peakfinding algorithm similar to the one discussed in Li & Fenimore 1996 (see Appendix A for more details). For approximately, 4 per cent, 7 per cent, and 11 per cent of uniform random realizations for the  $e=0.3,\,0.45,\,$  and 0.6, respectively, the polarization curves exhibit only a single peak. These single-peak cases have been excluded from the statistical analysis of PPA rotation presented in Figs 3–5.

Single-peak behaviour can be understood from the simple configuration where the line of sight passes through the jet centre (i.e. the origin; see Fig. 1 for the following discussion). The visible region forms a ring centred at this point, with each fluid element emitting polarized light in the local radial direction. For a circular jet

head (e=0), the system's symmetry leads to complete cancellation of the polarization signal. In contrast, for an eccentric jet head  $(e \neq 0)$ , the initial net polarization is zero, but as the jet decelerates, the top and bottom parts of the ring, emitting vertically polarized light, extend beyond the jet edge, breaking the symmetry. The net polarization then becomes dominated by the left and right parts of the ring, whose emission is polarized in the horizontal direction. As deceleration proceeds, these segments continue to dominate, resulting in a constant PPA and a single peak in the polarization curve. Although the probability of the line of sight passing exactly through the jet centre is zero, we find that the polarization curve still exhibits a single peak, accompanied by a rotation of the PPA, when the line of sight lies close to the centre. As the viewing angle increases, a minor bump typically emerges during the rising phase and gradually evolves into a two-peak structure.

#### 4 NON-AXISYMMETRIC STRUCTURED JET

Observations of GRB 170817A demonstrate that some GRB jets deviate from a simple top-hat structure, instead exhibiting a structured profile. To capture this complexity, we extend our model to incorporate a structured luminosity distribution. In this framework, a uniform central core is encircled by a fainter outer region, where the surface luminosity density gradually declines following a power-law profile, extending out to the jet's maximum opening angle.

We assume that the core, the jet edge and brightness contours all have a common elliptical shape with a common eccentricity e, where the jet core  $\theta_c$  and the jet outer edge angles  $\theta_j$  are defined along the semimajor axis. Considering the relativistic limb-brightening effect, we adopt the same ring-shaped visible region as in the top-hat jet case. The procedure for estimating polarization signals remains unchanged, but the local luminosity dL of a segment is now determined by a position-dependent surface luminosity density, which is highest in the core and decreases as a power law with index  $\alpha$  in the outer region.

The luminosity reduction factor for a segment in the outer region, located at (x, y) on the jet head is given by

$$\left(\frac{x^2}{a_0^2} + \frac{y^2}{b_0^2}\right)^{-\alpha/2}$$
, (5)

where  $a_c = \theta_c$  and  $b_c = \theta_c \sqrt{1 - e^2}$  are the semimajor and semiminor axes of the elliptical jet core.

In a structured jet, the jet break time for an off-axis observer is determined by the viewing angle  $\theta_{\text{view}}$ , rather than by the jet opening angle as in the top-hat jet model (Rossi, Lazzati & Rees 2002; Zhang & Mészáros 2002). We estimate the characteristic jet-break time  $t_j$  using a simple relation  $\Gamma(t_j) \sim 1/\theta_{\text{eff}}$ , where  $\theta_{\text{eff}} = \theta_{\text{view}}$  if the line of sight is in the outer region, and  $\theta_{\text{eff}} = \theta_{\text{c}}$  if it is within the core.

Fig. 6 shows the polarization signals when the line of sight falls in the outer region. As demonstrated by Rossi et al. (2004) and Birenbaum et al. (2024), the polarization curves differ significantly from those of a top-hat jet, regardless of axial symmetry. This discrepancy arises from the non-uniform luminosity distribution in the visible region surrounding the line of sight (i.e. the ring), with the intense emission concentrated towards the jet axis. Consequently, the observed polarization signal is primarily influenced by these bright segments, resulting in a single peak in the polarization curve.

The position angle evolution also differs from those of a top-hat jet. It consistently aligns with the direction towards the central jet axis (see assumption 4 in Section 2). When the line of sight falls on the jet head near its semimajor or semiminor axis ( $\chi \sim 0$  or  $\pi/2$ ), the geometry becomes more symmetric, the position angle remains

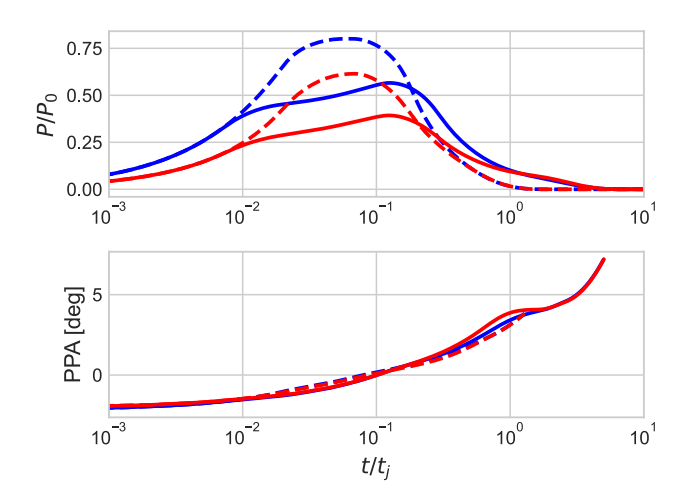


**Figure 6.** Polarization signals for a line of sight intersecting the outer region, where the surface luminosity density declines following a power law with an index of  $\alpha=2$  (red) or 3 (blue). Two offset angles are considered:  $\xi=2\theta_{\rm c}/\theta_{\rm j}$  (solid) and  $4\theta_{\rm c}/\theta_{\rm j}$  (dashed). Top panel: temporal evolution of polarization degree. Bottom panel: temporal evolution of polarization position angle. The model assumes e=0.3,  $\chi=\pi/4$ , and  $\theta_{\rm c}/\theta_{\rm j}=0.13$ .

constant over time, consistent with the results for axisymmetric structured jets (Rossi et al. 2004). However, for a general azimuthal angle  $\chi$ , the eccentricity of the brightness contour lines leads to a slight evolution of the position angle around the peak of the polarization degree. This effect is illustrated for  $\chi=\pi/4$  in the bottom panel of Fig. 6.

The PPA rotation over the full width at half-maximum of the polarization peak is evaluated for  $\chi=\pi/4$  (the rotation is maximized for  $\chi=\pi/4$ ). We obtain rotation values of  $\Delta\phi=3.5, 2.9, 2.6$  deg for  $e=0.3, \ \Delta\phi=16, \ 13, \ 12$  deg for e=0.6, corresponding to  $\xi/\left<\theta_{\rm c}/\theta_{\rm j}\right>=2, 3, 4$ , respectively. While these values are evaluated for  $\alpha=3$ , the rotation remains insensitive to  $\alpha$ .

As discussed in Section 3, the polarization degree curve can exhibit a single peak even for top-hat, non-axisymmetric jets when the line of sight is close to the jet axis. In such cases, the PPA typically rotates between a minor bump and the main peak, reaching a local maximum or minimum at the peak of the polarization curve. The rotation rate of the PPA often differs markedly between the rising and decaying phases. In contrast, for structured jets, the PPA evolves more smoothly and continuously across the peak.

Fig. 7 illustrates polarization signals when the line of sight passes through the jet core, corresponding to  $\xi=0.5(\theta_c/\theta_j)$  and  $\chi=\pi/4$ . The polarization curves resemble those of top-hat, non-axisymmetric jets (represented by the red solid line in the top panel of Fig. 2), exhibiting two peaks without a complete polarization dip in between. The temporal evolution of the PPA (shown in the bottom panel) is largely insensitive to the value of  $\alpha$ . When  $\alpha=2$  and 3, we obtain the PPA rotation between the two peaks is  $\Delta\phi\sim79$  and 80 deg, respectively. In the limit  $\alpha\gg1$  (i.e. the top-hat model), the rotation angle increases slightly to  $\Delta\phi\sim83$  deg. Overall, the top-hat model serve as a reasonable approximation of the polarization signals when the line of sight intersects the jet core.

# 5 CASE STUDIES

Optical linear polarization measurements have been conducted for many GRB afterglows, typically several hours to a few days after the prompt gamma-ray emission (Covino & Gotz 2016, and references

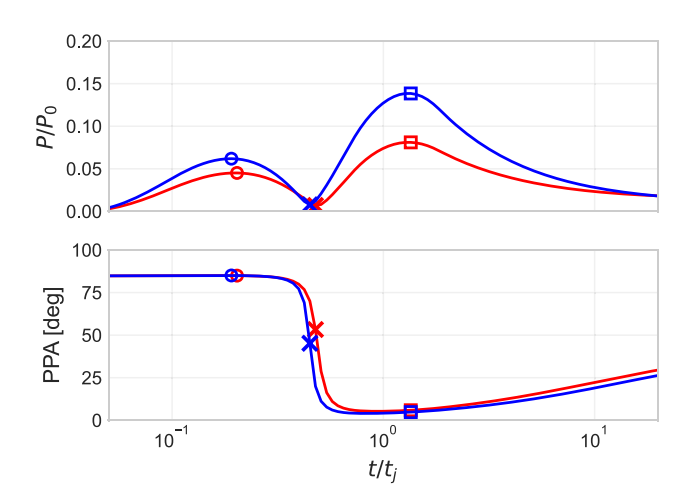


**Figure 7.** Polarization signals for a line of sight intersecting the jet core at  $\xi = 0.5\theta_{\rm c}/\theta_{\rm j}$ . All jet properties are identical to those in Fig. 6, except where specified. Top panel: polarization degree curves. Bottom panel: evolution of the polarization position angle. Curves are shown for  $\alpha = 2$  (red) and  $\alpha = 3$  (blue). The first peaks, the troughs and second peaks in the polarization light curves are marked by circles, crosses, and squares, respectively.

therein). This time frame corresponds to when a jet break is expected to occur. The observed linear polarization degree or its upper limits are generally low ( $\stackrel{<}{\sim}$  several percent). Such low polarization levels suggest that in shock-generated random magnetic fields, neither the component parallel nor perpendicular to the shock normal dominates entirely (e.g. Gill & Granot 2020), though the fields are not fully isotropic. In our model, the local polarization degree  $P_0$  is treated as a free parameter that sets the overall normalization of the polarization curve but it does not affect its shape or the absolute values and evolution of PPA. Adopting a low value,  $P_0 \ll 0.7$  (much smaller than the maximum value for ordered fields), makes the model well suited for interpreting afterglow polarization measurements.

# 5.1 GRB 020813

A bright long-duration burst (> 125 s) detected by HETE-2, located at a redshift of z = 1.255 (Barth et al. 2003), was studied. Polarimetry data obtained with Keck and VLT (Gorosabel et al. 2004) was collected around a jet break, occurring at  $\sim 13$  h post-burst (Covino et al. 2003). As shown in Fig. 8, the data is most consistently described by an almost constant degree of linear polarization at the  $\sim 1$  per cent level, along with a stable position angle. While a slow evolution of the position angle  $\Delta \phi \sim$  a few tens of degrees cannot be ruled out, the observations do not support a sudden 90 deg rotation of the position angle at the jet break, which is a signature of top-hat axisymmetric jets. Given the sparsity of polarization data points, a single-peaked polarization curve remains consistent with the observations. The evolution of both the polarization degree and position angle can be explained by structured jets, whether axisymmetric or not. If a gradual rotation of the position angle were confirmed, it would indicate a structured, non-axisymmetric jet.

# 5.2 GRB 091018

This long burst ( $T_{90} = 4.4$  s and redshift z = 0.971) was detected by Swift (Wiersema et al. 2012). Its optical light curve is well described by a broken power law, with a break at  $\sim 9$  h, coinciding with a steepening in the X-ray light curve. While the post-break decay indices (1.54 in the X-ray and 1.33 in the optical) are shallower than

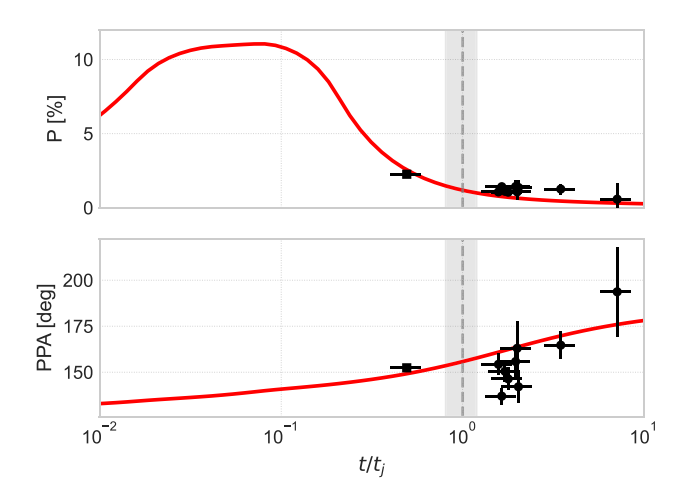


**Figure 8.** Sample fit for GRB020813 (red solid line). Structured jet model parameters: e = 0.6,  $\theta_c/\theta_j = 0.13$ ,  $\xi = 3(\theta_c/\theta_j)$ ,  $\chi = 0.8$ , and  $P_0 = 0.15$ . Optical polarimetry data from (Gorosabel et al. 2004) are shown, where squares (pre-break) and circles represent Keck and VLT measurements, respectively. The time axis is normalized to the break  $t_j = 0.56 \pm 0.21$  d detected in the V-band light curve, with the break-time uncertainty indicated by the shaded region.

predicted from the standard fireball model, similar trends have been observed in other *Swift* XRT afterglows, where potential jet breaks often exhibit relatively shallow decay indices (Racusin et al. 2009).

Linear polarization monitoring with VLT (Wiersema et al. 2012) revealed a polarization curve inconsistent with a single-peaked profile, and instead favouring a two-peak structure. In top-hat jet models, both axisymmetric and non-axisymmetric, the second peak tends to have a higher amplitude than the first. Although some data points support this trend, significant scatter suggests the presence of a deep, short dip within the second peak. The PPA remains stable and nearly constant during the first peak, but shifts to a higher overall value in the second peak, with significant scatter around the 90-deg rotation. These variations in both the polarization degree and position angle during the second peak are not fully explained even by nonaxisymmetric jets (i.e. elliptical jet heads). As noted by Wiersema et al. 2012, if the scatter in the second peak is caused by an additional component such as a bright patch within the jet or microlensing effects that partially cancel the polarization signals, the presence of a two-peak profile, combined with a nearly constant PPA in the first peak, suggests either a top-hat jet or a view of the core of a structured jet. In this scenario, the jet head (or core) must have a small eccentricity or be observed from a line of sight located near its semimajor or semiminor axis. Additionally, the shallow post-break decay indices may imply that the jet core is encased by an outer region with a shallow angular profile.

# 5.3 GRB 121024A

A long burst with  $T_{90} = 69$  s was detected by *Swift*, with a redshift of z = 2.298 determined shortly afterwards. The X-ray light curve follows a three-segment power-law evolution, with the final break at  $t \sim 10$  h coinciding with a break in the optical light curve (Wiersema et al. 2014). The monochromatic nature of this break suggests a jet break origin. However, the post-break decay indices remain relatively shallow, at 1.67 in the X-rays and 1.25 in the optical. VLT polarimetry measurements taken 3–6 h after the burst show linear polarization degrees ranging from 3 per cent to 5 per cent, with a stable position angle (see Fig. 10). However, observations from the following

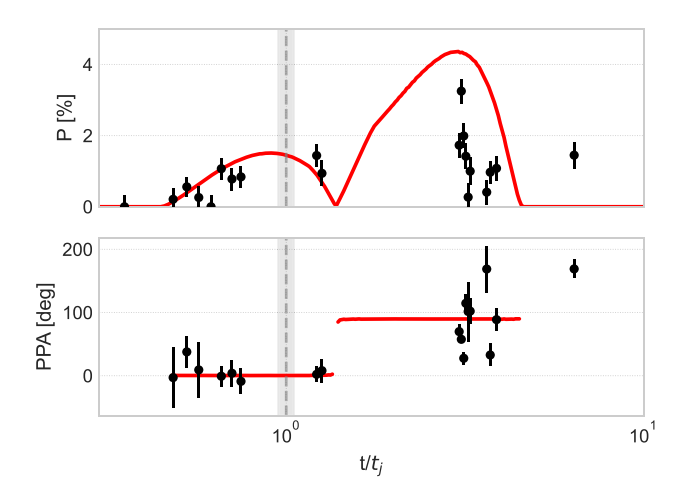


**Figure 9.** Sample fit for GRB091018 (red solid line). Top-hat jet model parameters: e = 0.15,  $\xi = 0.25$ ,  $\chi = -1.48$ , and  $P_0 = 0.15$ . Optical polarimetry data from (Wiersema et al. 2012).

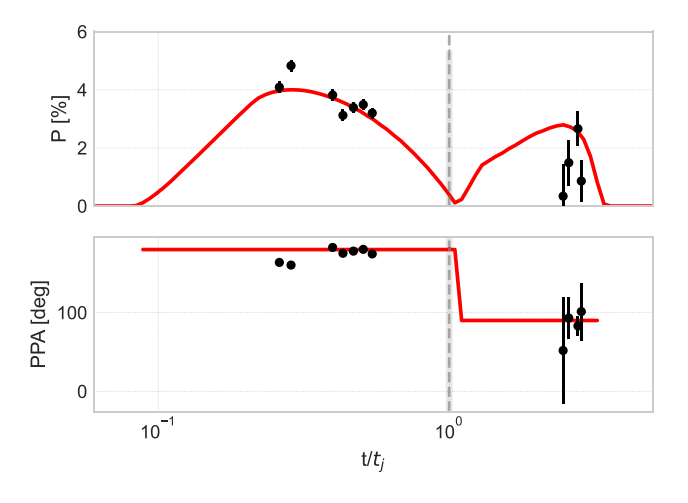


**Figure 10.** Sample fit of GRB121024A (red solid line). Top-hat jet model parameters: e = 0.65,  $\xi = 0.35$ ,  $\chi = \pi/2$ , and  $P_0 = 0.22$ . Optical polarimetry data from (Wiersema et al. 2014).

night (after the jet break) reveal a significant shift in the position angle, consistent with a 90 deg rotation (Wiersema et al. 2014). These polarization properties also support the similar jet structure interpretations as for GRB 091018, although the polarization degree shows significant scatter (with larger uncertainties) after the break (the top panel), and our model curve does not reproduce these data well in this case either.

#### 5.4 GRB 210610B

A long-duration burst at z=1.134 was detected by Fermi ( $T_{90}=69\,\mathrm{s}$ ) and Swift ( $T_{90}=55\,\mathrm{s}$ ). The optical and X-ray light curves are modelled using a broken power law. The optical light curve remains initially flat until the break at  $\sim 7.8\,\mathrm{h}$ , after which it steepens to a decay index of 1.85. The X-ray light curve appears to undergo a simultaneous break and shares the same post-break decay index, though its pre-break decay is faster than that of the optical counterpart (Agüí Fernández et al. 2024). Polarimetric observations were conducted with the Calar Alto Telescope and the VLT. The first measurements, taken at around 2.9 h, revealed a relatively high polarization degree of  $\sim 4.5\,\mathrm{per}$  cent as shown in Fig. 11. During

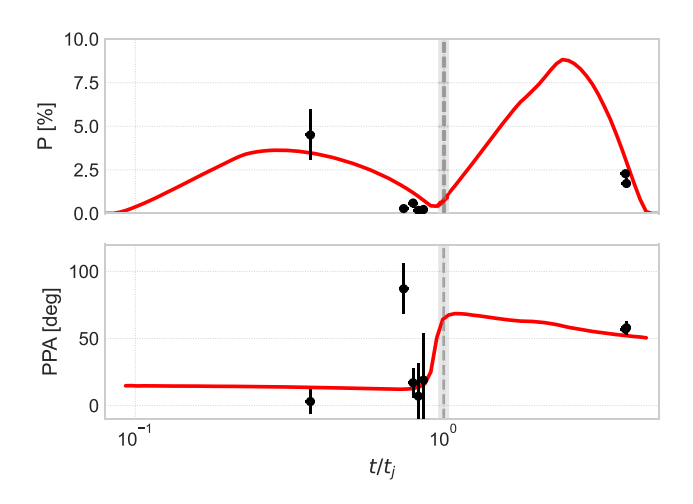


**Figure 11.** Sample fit of GRB210610B (red solid line). Top-hat jet model parameters:  $e = 0.7, \xi = 0.35, \chi = -1.1$ , and  $P_0 = 0.2$ . Optical polarimetry data from (Agüí Fernández et al. 2024).

the second observation period (5.8–6.7 h), which is close to the break time, the polarization level dropped significantly to 0.18-0.6 per cent. However, after the break, the polarization degree increased again to  $\sim 2\,$  per cent (30.4–30.6 h). Interestingly, the PPA rotates by 54 deg between the pre- and post-break measurements (the bottom panel), suggesting a significant shift that deviates notably from the 90 deg rotation expected for axisymmetric jets.

This event is a strong candidate for modelling with a nonaxisymmetric jet. Here, we assume top-hat, non-axisymmetric jets for our analysis. While a structured, non-axisymmetric jet could also explain the event if the line of sight intersects the jet core, the constraint on the jet head's eccentricity remain similar. Given the large deviation of  $|\Delta \phi - \pi/2| = 36 \deg$ , and the distinct trough structure  $R_{\rm pd} \ge 10$ , we performed 5000 random samplings. For a lower eccentricity (e = 0.3), most cases (87 per cent) yield  $R_{pd} > 10$ . However, virtually none satisfy  $|\Delta \phi - \pi/2| > 36$  deg. For e = 0.75, the fraction of cases meeting the first, second, and both conditions are 64 per cent, 35 per cent, and 21 per cent, respectively. The lines of sight that satisfy both conditions are characterized by intermediate azimuthal angles:  $0.4 < \chi < 1.5$  and a relatively central region:  $\xi$  < 0.7. These findings suggest this event could be explained within a non-axisymmetric jet framework. However, there are caveats in the jet-break modelling. (1) The flat optical light curve before the break suggests significant energy injection into the forward shock at early times. Since ejecta from the central engine can carry large-scale magnetic fields (Mundell et al. 2013) unlike forward shocks, which generates highly tangled magnetic fields, the polarization signals before the break may be significantly influenced by emission from refreshed shocks (energy injection). (2) The post-break decay index of the optical afterglow (1.85  $\pm$  0.04) is close to, but still shallower than, the expected value ( $\sim$  2) for the standard fireball model (Agüí Fernández et al. 2024).

## 6 CONCLUSIONS

We have investigated the afterglow polarization signals around a jet break for non-axisymmetric jets. For jets with top-hat luminosity density distributions, the polarization degree curves exhibit two peaks in general, even when the jet head is elliptical. However, a complete polarization drop between the peaks is generally absent. Unlike axisymmetric jets, where the PPA undergoes a sudden jump at the trough, the PPA in non-axisymmetric jets evolves smoothly. Additionally, the change in PPA between the two peaks can deviate significantly from 90 deg. In our random line of sight sampling, 50 per cent of the cases show deviations of more than 18 deg, and 10 per cent exceed 31 deg for e = 0.6.

If the jet's luminosity density gradually declines following a power-law profile, the polarization curves exhibit a single peak. We find the shapes of the curves are similar for  $\alpha = 2$  and 3. In this structured jet case, the PPA can show a slight evolution for non-axisymmetric jets, in contrast to a constant PPA expected in axisymmetric jet models. Over the full width at half-maximum of the polarization peak, the PPA rotates by  $16 \deg$  for e = 0.6 with a line of sight at  $\chi = \pi/4$  and  $\xi = 2(\theta_c/\theta_i)$ . The results remain consistent for  $\alpha = 2$  and 3.

For structured, non-axisymmetric jets, in which a uniform central core is surrounded by an outer region with a power-law luminosity profile, the polarization signals depends on the line of sight location. This model can account for a wide range of polarization behaviours, as discussed in the case study section. When the line of sight intersects the uniform jet core, the signals resemble those of tophat jets. If the line of sight passes through the jet head - whether in the core or outer region - near its semimajor or semiminor axis, the geometry becomes more symmetrical, making the polarization signals of non-axisymmetric jets similar to those of axisymmetric iets. Significant deviations in the PPA rotation from 90 deg (or from a constant PPA in the case of a structured jet) arise when the line of sight has an intermediate azimuthal angle ( $\chi \sim \pi/4$ ) and a relatively small offset angle ( $\xi \lesssim 0.4$ ), i.e. when it is close to the jet

As a simple toy model for a structured jet, we considered a case where the luminosity density in the jet's outer region follows a power-law profile. While this simplified model should captures the key features of polarization signals in structured jets, the angular dependence of luminosity density in a more realistic scenario arises from the lateral energy distribution - where the jet core has a higher energy per solid angle, and the outer regions gradually contain less energy per solid angle. This also induces the angular variations in the Lorentz factor, with the core having a higher Lorentz factor and progressively decreasing toward the outer regions. As a result, the visible region is no longer circularly symmetric, towards the jet centre, the relativistic beaming is stronger and luminosity contribution is larger (e.g. fig. 2 in Beniamini, Gill & Granot 2022). The impact of this deformed visible region will be explored in a future paper.

When constructing the polarization degree light curves shown in Figs 2, 6–11, we assumed the forward shock dynamics  $\Gamma \propto t^{-3/8}$ for the interstellar medium (ISM). In the wind medium, the curve shapes are slightly modified due to different forward shock dynamics  $\Gamma \propto t^{-1/4}$ . However, the overall morphology (e.g. the presence of two peaks or a single peak) remains unchanged and the discussion on  $\Delta\phi$ should be similar.

If the jet head has a highly eccentric shape, it can be characterized by two angular scales:  $\theta_i$  (the opening angle along the semimajor axis) and  $\theta_{i2}$  (along the semiminor axis). As long as  $\Gamma > 1/\theta_{i2}$ , the flux follows the typical blast wave emission evolution, decaying approximately as  $t^{-1}$ . When  $\Gamma \propto t^{-3/8}$  drops below this first critical threshold, photons begin to be emitted over a larger solid angle, increasing from  $\theta_i \theta_{i2}$  to  $\Gamma^{-1} \theta_i$ , causing the flux to decay as  $t^{-11/8}$ . As  $\Gamma$  continues to decrease and falls below the 2nd threshold  $1/\theta_i$ , the emission solid angle expands further to  $\Gamma^{-2}$ , leading to a steeper decay of  $t^{-7/4}$ . Since these breaks arise from geometrical effects, they are expected to be monochromatic, similar to the usual jet break. The two jet break times  $t_i$  and  $t_{i2}$ , with  $t_{i2} < t_i$ , satisfy the relation

$$t_{i2}/t_i \sim (1-e^2)^{4/3}$$
. (6)

For axisymmetric jets (e = 0), it simplifies to the standard single jet break. For a mildly deformed jet head with e = 0.6, the ratio is approximately  $t_{i2}/t_i = 0.55$ . As a result, the breaks will appear as a smooth transition rather than two distinct ones. While we have assumed a top hat-jet in the ISM to estimate the break time ratio, a wind-like medium would further smooth out each break (Panaitescu & Kumar 2000), making them appear as single gradual break. Detecting these breaks in a light curve (requiring  $t_{i2}/t_i \ll 1$ ) would allow for an estimate of the jet's eccentricity as

$$e \sim \sqrt{1 - (t_{j2}/t_j)^{3/4}}.$$
 (7)

A more detailed discussion of jet breaks in light curves, including estimates for non-axisymmetric structured jets, will be investigated in a future study.

Although our case study section focused on optical afterglow observations, the jet break is a geometrical effect, meaning our results are applicable across different wavelengths (e.g. X-ray, radio). The number of events with measured radio polarization has recently increased (Corsi et al. 2018; Laskar et al. 2019; Urata et al. 2019, 2023). Significant advancement in X-ray polarimetry in recent years (e.g. Astrosat, IXPE, POLAR, XPoSat) suggest that future X-ray satellites may be capable of detecting and analysing polarization signals days after GRBs. Since both X-ray and optical bands are expected to lie above the typical frequency of the forwards shock emission around jet breaks, the relativistic limb-brightening effect should be pronounced in both bands (Granot et al. 1999).

We adopted a conventional scenario in which magnetic fields are amplified by plasma kinetic instabilities at the shock, resulting in a coherence length scale comparable to the plasma skin depth scale (Medvedev & Loeb 1999). Recently, large-scale turbulent magnetic fields driven by magnetohydrodynamic instabilities have also been proposed (e.g. Kuwata et al. 2023). In this scenario, the coherence length-scale is comparable to the thickness of the blast wave. In the isotropic field case, both the polarization degree and the PPA change randomly and continuously over time, resembling the behaviour described in the classical patch shell model (e.g. Gruzinov & Waxman 1999; Nakar & Oren 2004). By incorporating magnetic field anisotropy and the observer's viewing angle, this model can also account for a variety of polarization behaviour in afterglows. Notably, in this framework, the degree of radio polarization can exceed that in the optical band (Kuwata et al. 2024). Simultaneous polarimetric observations across multiple wavelengths will be crucial for constraining the magnetic field amplification mechanism and improving our understanding of polarization signals in afterglows.

#### **ACKNOWLEDGEMENTS**

We thank the anonymous referee for their constructive comments and suggestions, which have helped to improve the manuscript. We are also grateful to Gavin P. Lamb for useful discussions. This research was supported by the Science and Technology Facilities Council (STFC) grants.

### DATA AVAILABILITY

The data underlying this article will be shared on reasonable request to the corresponding author.

#### REFERENCES

```
Abbott B. P. et al., 2017, ApJ, 848, L12
Agüí Fernández J. F. et al., 2024, A&A, 690, A216
Barth A. J. et al., 2003, ApJ, 584, L47
Benjamini P., Gill R., Granot J., 2022, MNRAS, 515, 555
Birenbaum G., Gill R., Bromberg O., Beniamini P., Granot J., 2024, ApJ,
   974, 308
Burns E. et al., 2023, ApJ, 946, L31
Corsi A. et al., 2018, ApJ, 861, L10
Covino S., Gotz D., 2016, A&A, 29, 205
Covino S. et al., 2003, A&A, 404, L5
Ghirlanda G. et al., 2019, Science, 363, 968
Ghisellini G., Lazzati D., 1999, MNRAS, 309, L7
Gill R., Granot J., 2020, MNRAS, 491, 5815
Gill R., Granot J., 2024, MNRAS, 527, 12178
Gorosabel J. et al., 2004, A&A, 422, 113
Gottlieb O., Nakar E., Bromberg O., 2021, MNRAS, 500, 3511
Gottlieb O., Moseley S., Ramirez-Aguilar T., Murguia-Berthier A., Liska M.,
   Tchekhovskoy A., 2022, ApJ, 933, L2
Granot J., Piran T., 2012, MNRAS, 421, 570
Granot J., Piran T., Sari R., 1999, ApJ, 513, 679
Gruzinov A., Waxman E., 1999, ApJ, 511, 852
Huang B.-Q., Lin D.-B., Liu T., Ren J., Wang X.-G., Liu H.-B., Liang E.-W.,
   2019, MNRAS, 487, 3214
Kuwata A., Toma K., Kimura S. S., Tomita S., Shimoda J., 2023, ApJ, 943,
   118
Kuwata A., Toma K., Tomita S., Shimoda J., 2024, ApJ, 977, 224
Lamb G. P., Kobayashi S., 2017, MNRAS, 472, 4953
Lamb G. P. et al., 2019, ApJ, 870, L15
Lamb G. P., Nativi L., Rosswog S., Kann D. A., Levan A., Lundman C.,
   Tanvir N., 2022, Universe, 8, 612
Laskar T. et al., 2019, ApJ, 878, L26
Lazar A., Nakar E., Piran T., 2009, ApJ, 695, L10
Lazzati D., Begelman M. C., 2005, ApJ, 629, 903
Lazzati D., Perna R., Morsony B. J., Lopez-Camara D., Cantiello M.,
   Ciolfi R., Giacomazzo B., Workman J. C., 2018, Phys. Rev. Lett., 120,
   241103
Lesage S. et al., 2023, ApJ, 952, L42
Li H., Fenimore E. E., 1996, ApJ, 469, L115
Li J.-D., Gao H., Ai S., Lei W.-H., 2023, MNRAS, 525, 6285
Li J.-D., Gao H., Ai S., Lei W.-H., 2024, ApJ, 978, 124
Margutti R. et al., 2018, ApJ, 856, L18
Medvedev M. V., Loeb A., 1999, ApJ, 526, 697
Mundell C. G. et al., 2013, Nature, 504, 119
Nakar E., Oren Y., 2004, ApJ, 602, L97
Nativi L., Lamb G. P., Rosswog S., Lundman C., Kowal G., 2022, MNRAS,
   509, 903
O'Connor B. et al., 2023, SciA, 9, eadi1405
Panaitescu A., Kumar P., 2000, ApJ, 543, 66
```

```
Perego A., Rosswog S., Cabezón R. M., Korobkin O., Käppeli R., Arcones A., Liebendörfer M., 2014, MNRAS, 443, 3134

Racusin J. L. et al., 2009, ApJ, 698, 43

Rossi E., Lazzati D., Rees M. J., 2002, MNRAS, 332, 945

Rossi E. M., Lazzati D., Salmonson J. D., Ghisellini G., 2004, MNRAS, 354, 86

Sari R., 1999, ApJ, 524, L43

Sari R., Piran T., Narayan R., 1998, ApJ, 497, L17

Stringer E., Lazzati D., 2020, ApJ, 892, 131

Troja E. et al., 2019, MNRAS, 489, 1919

Urata Y. et al., 2019, ApJ, 884, L58

Urata Y. et al., 2023, Nat. Astron., 7, 80

Wiersema K. et al., 2012, MNRAS, 426, 2

Wiersema K. et al., 2014, Nature, 509, 201

Zhang B., Mészáros P., 2002, ApJ, 571, 876
```

#### APPENDIX: PEAK FINDING ALGORITHM

Zhang W., Woosley S. E., MacFadyen A. I., 2003, ApJ, 586, 356

To identify peaks and their locations in numerical polarization curves, we use a peak-finding algorithm similar to the one discussion in Li & Fenimore 1996. Originally developed for identifying peaks in prompt gamma-ray light curves, this method is well suited for our analysis. The detailed procedure is as follows: (1) A numerical polarization curve consists of discrete data points, representing the polarization degree (percent) as a function of time. A data point is considered a candidate peak if its value is higher than that of its neighbouring points on both sides. The candidate peak has a polarization degree  $P_p$  (percent) at time  $t_p$ . (2) For each candidate peak, we search both sides to identify data points with polarization degree  $P_1$  at  $t = t_1 < t_p$  and  $P_2$  at  $t = t_2 > t_p$  that satisfy the conditions

$$P_{\rm p} - P_i \ge N_v \sqrt{P_{\rm p}},\tag{A1}$$

where i = 1, 2 and  $N_v = 5$ . (3) The search stops when either: both  $P_1$  and  $P_2$  are found, confirming  $P_p$  as a true peak, or a polarization degree higher than  $P_p$  is encountered before finding a data point satisfying equation (A1) on either side of  $t_p$ , in which case  $P_p$  is discarded as a false peak.

After this step, all the peaks (one or two peaks in our case) should have been identified. If two peaks are found, the minimum point between them is designated as a trough. This method effectively identifies peaks in polarization curves while mitigating the effects of small fluctuations due to numerical errors, including the segmentation of the jet head.

This paper has been typeset from a TEX/LATEX file prepared by the author.